Optical-and-Radar Image Fusion for Dynamic Estimation of Spin Satellites

Yejian Zhou, Lei Zhang, Yunhe Cao, and Yan Huang

***Abstract*— As more and more satellites are launched into the space, dynamic estimation of spin satellites has become a critical component of the space situation awareness application. Some explored studies using exterior measurements from different sensors such as optical device and inverse synthetic aperture radar (ISAR) to estimate dynamic parameters of spin satellites. As a single sensor normally provides two-dimensional observation, three-dimensional estimations resulting from these algorithms are strictly related to the prior knowledge of targets characteristics. As a result, it is difficult to expand these methods to other satellites. In order to support the dynamic estimation of most spin satellites, this paper presents a novel dynamic estimation approach which employs synchronized optical-and-radar images. The optical-and-radar fusion strategy has demonstrated its superiority in image analysis field, and breaks down the dynamic estimation of spin satellites into two sub-problems: target attitude estimation and spin parameters estimation. In this work, the proposed algorithm deduces two explicit expressions of target dynamic parameters under the imaging projection model of the joint optical-and-radar observation. Through the particle swarm optimization (PSO), target dynamic parameters are determined in two stages. This paper presents some experiments illustrating the feasibility of the proposed method and subsequent conclusions, which reflect advantages of the joint optical-and-radar observation mode in image interpretation.**

***Index Terms*— Dynamic estimation, spin satellites, optical-and-radar fusion, image interpretation.**

I. Introduction

DYNAMIC estimation of spin satellites is of high importance for various space situation awareness (SSA) applications. It helps observers monitor satellite's health state and avoid potential space collisions, particularly for decommissioned satellites. After a decommissioned satellite loses contact with the ground, it is out of control in the space environment. Due to its gravity-gradient torque, it tumbles and then maintains spinning for a long time [1]–[3]. Once it stops conveying data to the ground, most ego-motion estimation methods for determining its motion state cannot work, whether it is based on the measuring system or observation data [4]–[7]. Therefore, the exterior measurement implemented by remote sensing devices is normally used to acquire dynamic parameters in this condition.

Most existing studies are based on the interpretation of observation data from single sort of sensor [8]–[20]. For example, supported by International Laser Ranging Service (ILRS), the relevant research activity was implemented to track the Envisat from 2013 to 2015 through global satellite laser ranging (SLR) stations. By matching this historical database, the current measurement of the range residual (the relative position of the corner cube reflectors (CCR) mounted on the satellite) was employed to determine its spin parameters [1], [10], [11]. However, this data-driven strategy can hardly be extended to other satellites without CCR mounted in advance or lacking long-term historical data. In Ref. [15], [16], another typical method was based on inverse synthetic aperture radar (ISAR) imaging technique. The measured image was matched to a target three-dimensional (3D) model to estimate its attitude information, but it relied on the prior knowledge of the target spin pattern for the image azimuth scaling. Without the prior knowledge, it is hard to obtain enough 3D information to determine satellite dynamic parameters from a single two-dimensional (2D) image because both optical and radar imaging processing can be regarded as the target projection from 3D place to 2D imaging plane [21]–[23]. It means beside the 2D single-sensor image, the dynamic estimation of satellites needs the support of additional information. The alternative approach proposed in this work is the joint optical-and-radar observation. In recent decades, it has been shown that optical-and-radar fusion strategy has dramatically superiority for many challenging works in image analysis field, such as urbanization monitoring and target recognition [24]–[30]. For example, the experiments in Ref. [24] demonstrated optical-and-radar observations considerably enhance the performance of multi-object tracking over a single sensor system.

Inspired by these relevant literatures, a joint optical-and-radar observation strategy is adopted to estimate dynamic parameters of spin satellites in this paper. In fact, the crux of this task is to decouple the attitude estimation and spin parameters estimation of the satellite target. And the joint optical-and-radar observation is exactly an accessible way. After exploring the intrinsic connection between the observation

Manuscript received May 14, 2019; revised September 4, 2019 and October 8, 2019; accepted November 17, 2019. Date of publication November 28, 2019; date of current version January 28, 2020. This work was supported in part by the National Natural Sciences Foundation of China under Grant 61771372 and Grant 61771367 and in part by the National Science Foundation of Shanghai under Grant 1428700. The associate editor coordinating the review of this manuscript and approving it for publication was Prof. Guo-Jun Qi. *(Corresponding author: Lei Zhang.)*

Y. Zhou and Y. Cao are with the National Laboratory of Radar Signal Processing, Xidian University, Xi'an 710071, China, and also with the Collaborative Innovation Center of Information Sensing and Understanding, Xidian University, Xi'an 710071, China.

L. Zhang is with the School of Electronics and Communication Engineering, Sun Yat-Sen University, Guangzhou 510275, China (e-mail: zhanglei57@mail.sysu.edu.cn).

Y. Huang is with the State Key Laboratory of Millimeter Waves, Southeast University, Nanjing 210096, China.

Digital Object Identifier 10.1109/TIP.2019.2955248

radar imagery and target dynamic, the instantaneous attitude estimation of the target is divided from dynamic estimation, while residual dynamic parameters are related to the Doppler information in the radar imagery. Hence, the optical sensor is introduced to estimate target attitude by building a synchronized optical-and-radar observation system, which provides 3D target information during each coherent processing interval (CPI) of radar imaging. Different other optical and radar fusion strategies [24]–[30], this system focuses on the most fundamental characteristic of target structures, the projected lengths of some typical features and determines their attitudes in 3D space by the interpretation of observation images. Once the attitude information is acquired with the accommodation of the particle swarm optimization (PSO) algorithm [31]–[33], the Doppler information is taken into estimating relative motion between the radar and target. After eliminating the contribution of target trajectory, satellite spin parameters are determined according to the estimation result of the relative motion.

Compared with the existing methods, the proposed algorithm has some innovations.

1) Most existing methods use the long-time observation sequence to estimate satellite dynamic, while the proposed algorithm can determine target dynamic parameters through interpreting a pair of synchronized optical and radar images in a single CPI. It means that the proposed algorithm overcomes the limitation of observation scope on the ground in the dynamic estimation of spin satellites. Compared with conventional methods, it does not need long-term historical data of the satellite, which offers the possibility of accessing the dynamic monitoring for most spin satellites. For stable attitude satellites, it is also suitable for determining instantaneous target attitude and geometry information by the attitude estimation method proposed in this paper.
2) Another contribution is designing the optical-and-radar joint observation system for the sake of space applications. Essentially, the observation information of these two sorts of sensors are complementary from the same observation angle: radar records the ranging measurement of the target while the optical imaging plane is perpendicular to its line of sight (LOS). As a result, 3D target information is readily interpreted from the synchronized optical-and-radar images. Detailed discussion of the superiority of this joint observation system is given in the Experiment Part. This multiple-sensor fusion strategy is an alternative way to meeting various demands in image processing field.

The remainder of the paper is organized as follows. Section II introduces the fundamental of the proposed algorithm, and the imaging geometry of the optical-and-radar joint observation is also developed. Section III describes the proposed algorithm with four detailed steps, including image preprocessing, feature extraction, target attitude estimation, and spin parameter estimation. Section IV demonstrates the feasibility of the proposed algorithm by simulation experiments. Some conclusions of this work are drawn in Section V.

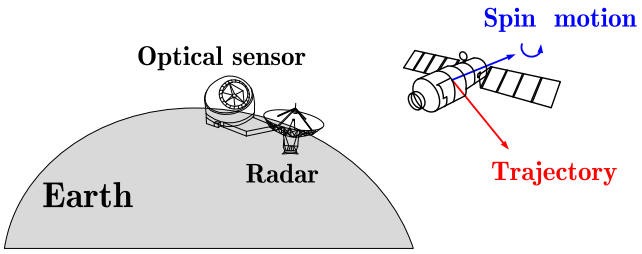

Fig. 1. The imaging geometry of the optical-and-radar joint observation.

II. The Estimation Model

In this section, the spin model of a on-orbit satellite and the geometric model of the optical-and-radar observation are introduced. Adopting synchronized optical-and-radar imaging, the connection between target image features and its dynamic parameters is derived with explicit expressions. Then, the dynamic estimation model of spin satellites is presented through jointly interpreting these multi-sensor images.

A. The Observation Geometry of Spin Satellites

The geometry model of the optical-and-radar joint observation is depicted in Fig. 1, where the radar and optical sensors are at a same observation station. During the passing of the satellite over the ground observation station, it is projected with different poses in radar and optical images due to different imaging mechanisms, though their perspective angles are same. Concretely, the imaging processing of the optical system depends on the affine phenomenon that the reflected ray of the target leaves a 2D shrunken image in the affine plane before arriving at the center of the optical sensor. By contrast, radar merely records the one-dimensional target distance history, and the other dimensional information depends on analyzing the frequency characteristics of the echo signal, also called Doppler analysis, in a single CPI. As a result, the imaging planes of these two sorts of sensors are different. In fact, they are perpendicular in each CPI, as shown in Fig. 2(a). The reason is that the affine plane, determined by the vertical and horizontal axes, is perpendicular to LOS, while one axis of the radar image is exactly the LOS direction at the central moment during the current CPI. The range axis of the radar image (i.e. the central LOS) is perpendicular to the vertical and horizontal axes of the optical image. Based on this three-dimensional perpendicular target information, the absolute attitude of the target can be estimated at the central moment of the current CPI, even though the target spins. After that, the other dimensional information in radar images, Doppler information, is to be used to estimate target dynamic parameters because target Doppler information has a close relationship with the relative motion between the radar and target.

In order to derive an explicit expression of this relationship in a certain coordinate system, the target Cartesian coordinate system is established to describe the target motion, as shown in Fig. 2(b). As a common coordinate system for monitoring satellite state [21]–[23], it is defined as below: X axis always points near the earth's core, Y axis is tangent to the

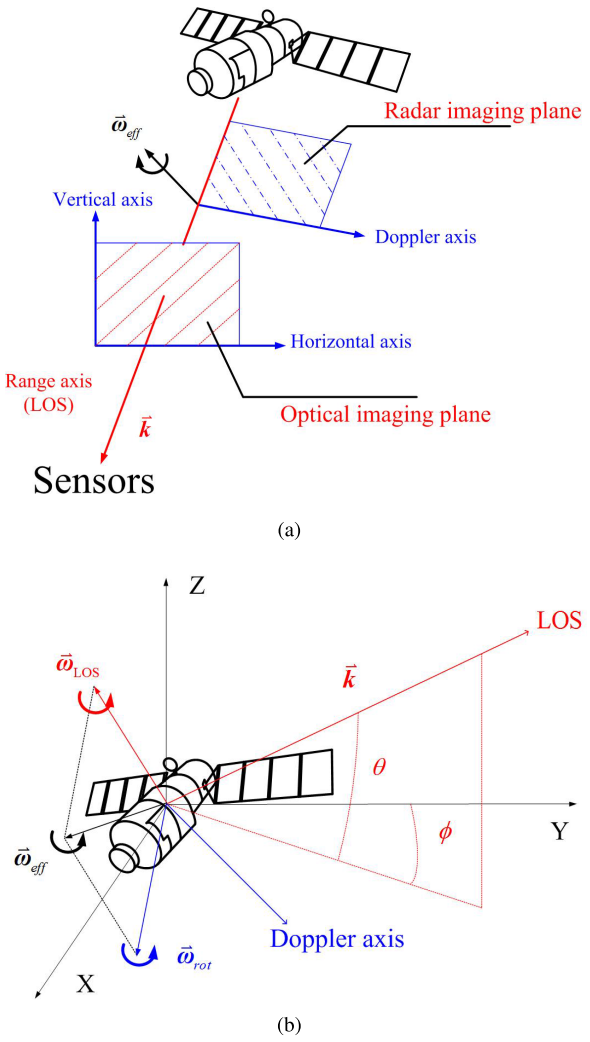

Fig. 2. The observation geometry and motion model of the spin satellite. (a) Target observation geometry in 3D world space. (b) Target spin model in the target Cartesian coordinate system.

target orbit and keeps up with the target trajectory motion, and Z axis is the normal direction of the target trajectory plane.

Under this coordinate system, instantaneous LOS is defined as a vector $\vec{\mathbf{k}}$ centered at the target position and oriented toward the ground station. It is determined by LOS parameters, elevation angle θ and azimuth angle ϕ, as in Eq. (1).

$$\vec{\mathbf{k}} = (\cos\theta\,(t_m)\sin\phi\,(t_m)\,,\cos\theta\,(t_m)\cos\phi\,(t_m)\,,\sin\theta\,(t_m))^{\mathrm{T}} \tag{1}$$

where t_m denotes the slow-time relative to the sampling in the azimuth direction, elevation angle $\theta\,(t_m)$ is the intersection angle between instantaneous radar LOS vector and the XOY plane, and azimuth angle $\phi\,(t_m)$ is the intersection angle between Y axis and the projection of instantaneous radar LOS vector in the XOY plane. When $t_m = t_0$, i.e. the central moment, the instantaneous LOS is consistent with the range axis of the radar image.

As shown in Fig. 1, the relative rotation between the target and each ground radar is caused by the trajectory and spin motion of the target, corresponding $\vec{\mathbf{w}}_{\mathrm{LOS}}$ and $\vec{\mathbf{w}}_{\mathrm{rot}}$ in Fig. 2(b) respectively.

$$\vec{\mathbf{w}}_{\mathrm{eff}} = \vec{\mathbf{w}}_{\mathrm{LOS}} + \vec{\mathbf{w}}_{\mathrm{rot}} \tag{2}$$

In this paper, an assumption is made that the target rotates around a certain rotation shaft with a constant speed in the current CPI. From relevant researches of Envisat [1], [10]–[12], the single CPI is generally reckoned at several seconds after taking the spin period of spacecraft (almost at the 160-second magnitude) and the trajectory motion of Low Earth Orbit (LEO) satellites into consideration. Therefore, this spin motion model is acceptable for instantaneous spin motion estimation. Different spin patterns of on-orbit satellites are simulated by changing the rotation shaft and speed during a long-term observation sequence in the later Experiment Part.

The spin component of the target is represented with a vector, namely

$$\vec{\mathbf{w}}_{\mathrm{rot}} = (\cos\theta_{\mathrm{rot}}\sin\phi_{\mathrm{rot}}, \cos\theta_{\mathrm{rot}}\cos\phi_{\mathrm{rot}}, \sin\theta_{\mathrm{rot}})^{\mathrm{T}}\omega_{rot} \tag{3}$$

where θ_{rot} and ϕ_{rot} are direction parameters of the rotation shaft, which are defined in the same way as LOS parameters, and ω_{rot} is the rotation speed.

Besides, it should be particularly emphasized that the spin vector $\vec{\mathbf{w}}_{\mathrm{rot}}$ corresponds to the central moment of the current CPI. Therefore, the range axis in the Range-Doppler (RD) image does not change under this motion model.

B. The Dynamic Estimation of Spin Satellites

This subsection introduces how to employ the synchronized optical-and-radar ISAR images to estimate the target attitude and spin parameters. First, target 3D information (in the vertical and horizontal dimensions of the optical image and range dimension of the radar image) is utilized to determine the target absolute attitude. Then, the Doppler dimension information of the radar image is employed for the estimation of target spin parameters. Detailed derivations are presented below.

Take the falling Chinese satellite, Tiangong-I (TG-I, NORAD catalog number 37820), for example. As shown in Fig. 3, two typical structural features, the spacecraft body and the solar wing, are projected in a RD imagery. The projection length of a typical structural feature on the range axis can be expressed as

$$r = \vec{\mathbf{k}}_{\mathrm{Radar,R}} \cdot \vec{\mathbf{l}} \tag{4}$$

$$\vec{\mathbf{l}} = L(\cos\alpha\sin\beta, \cos\alpha\cos\beta, \sin\alpha)^{\mathrm{T}} \tag{5}$$

where α and β represent attitude parameters of the typical structure, which are defined in the same way as LOS parameters, L refers to the 3D length of the typical structure, denotes the inner product, and $\vec{\mathbf{k}}_{\mathrm{Radar,R}}$ is the center LOS vector of the imagery.

Simultaneously, this structural feature is also projected in the optical image as

$$u = \vec{\mathbf{k}}_{\mathrm{Optical,U}} \cdot \vec{\mathbf{l}} \tag{6}$$

$$v = \vec{\mathbf{k}}_{\mathrm{Optical,V}} \cdot \vec{\mathbf{l}} \tag{7}$$

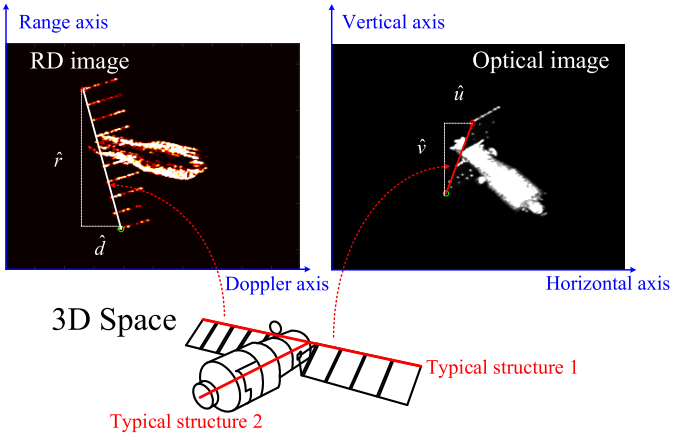

Fig. 3. The projection geometry of optical and radar imaging.

where the vertical and horizontal axes of optical are expressed by the direction vectors $\vec{\mathbf{k}}_{\text{Optical,V}}$ and $\vec{\mathbf{k}}_{\text{Optical,U}}$, respectively. These two vectors usually are recorded at the optical imaging moment (i.e. the central moment of radar imaging in this work), and assumed known in the later content.

Therefore, three-dimensional observation data is applied to estimate the attitude and length of each structural feature, namely

$$\begin{cases} \vec{\mathbf{k}}_{Radar,R} \cdot \vec{\mathbf{l}} = \hat{r} \\ \vec{\mathbf{k}}_{\text{Optical},U} \cdot \vec{\mathbf{l}} = \hat{u} \\ \vec{\mathbf{k}}_{\text{Optical},V} \cdot \vec{\mathbf{l}} = \hat{v} \end{cases} \tag{8}$$

where the superscript $\wedge$ refers to the measured value.

The observation Eq. (8) can be established for each typical structure independently, and converted to optimization (9), shown at the bottom of this page.

Optimization (9) can be solved in various ways. In this work, PSO is adopted to estimate the attitude and length parameters of each typical structure. The details are given in Section III.C.

According to the optimal $\left(\tilde{\alpha}, \tilde{\beta}, \tilde{L}\right)^T$, 3D vector of the typical structure can be calculated according to Eq. (10).

$$\tilde{\vec{\mathbf{l}}} = \tilde{L}\left(\cos\tilde{\alpha}\sin\tilde{\beta}, \cos\tilde{\alpha}\cos\tilde{\beta}, \sin\tilde{\alpha}\right)^{\mathrm{T}} \tag{10}$$

On the other hand, the unit vector of the Doppler axis $\vec{\mathbf{k}}_{Radar,Fd}$ is defined by the derivative of the radar distance. It means $\vec{\mathbf{k}}_{Radar,Fd}$ is always perpendicular to the range axis, while the radar range axis is also perpendicular to the optical imaging plane as mentioned above. Consequently, $\vec{\mathbf{k}}_{Radar,Fd}$ is the linear combination of the orthogonal basis of the optical imaging plane, the vertical and horizontal vectors, as

$$\vec{\mathbf{k}}_{Radar,Fd} = \cos\theta_{optical}\vec{\mathbf{k}}_{optical,v} + \sin\theta_{optical}\vec{\mathbf{k}}_{optical,u} \tag{11}$$

where $\theta_{optical}$ is the angle between the Doppler axis and the vertical axis. Similar to the interpretation processing of the projection length on radar range axis, the projection length of a structural feature on Doppler axis can be determined as

$$d = \omega_{eff}\vec{\mathbf{k}}_{Radar,Fd} \cdot \tilde{\vec{\mathbf{l}}} \tag{12}$$

where ω_{eff} refers to the equivalent rotation speed of LOS in the current CPI.

Once parameters $\vec{\mathbf{k}}_{Radar,Fd}$ and ω_{eff} are estimated, the equivalent radar LOS rotation $\vec{\mathbf{w}}_{\text{eff}}$ can be determined. Furthermore, the rotation of the target (i.e. $\vec{\mathbf{w}}_{\text{rot}}$) can also be calculated according to Eq. (2). Therefore, the later content in this subsection will focus on the estimation of parameters $\vec{\mathbf{k}}_{Radar,Fd}$ and ω_{eff}.

First, the projection length ratios of two structural features ought to be equal on the Doppler axis among synchronized optical-and-radar images.

$$\frac{\vec{\mathbf{k}}_{Radar,Fd} \cdot \vec{\mathbf{l}}_{optical,1}}{\vec{\mathbf{k}}_{Radar,Fd} \cdot \vec{\mathbf{l}}_{optical,2}} = \frac{\omega_{eff}\vec{\mathbf{k}}_{Radar,Fd} \cdot \vec{\mathbf{l}}_1}{\omega_{eff}\vec{\mathbf{k}}_{Radar,Fd} \cdot \vec{\mathbf{l}}_2} = \frac{d_1}{d_2} \tag{13}$$

where the projection of a structural feature in the optical imaging plane $\vec{\mathbf{l}}_{optical,i} = v_i\vec{\mathbf{k}}_{optical,v} + u_i\vec{\mathbf{k}}_{optical,u}$,and serial number $i = 1, 2$.

The ratio in the radar image is calculated directly by the measuring d_1 and d_2, while the ratio in the optical image is expressed as Eq. (14), shown at the bottom of this page.

It is converted to the following optimization, which is readily solved by PSO algorithm as well.

$$\min_{-\pi \le \theta_{optical} \le \pi} \left| \frac{\cos\theta_{optical}\hat{v}_1 + \sin\theta_{optical}\hat{u}_1}{\cos\theta_{optical}\hat{v}_2 + \sin\theta_{optical}\hat{u}_2} - \frac{\hat{d}_1}{\hat{d}_2} \right| \tag{15}$$

where $|*|$ indicates modulus operation.

According to the optimal $\tilde{\theta}_{optical}$, Doppler vector $\tilde{\vec{\mathbf{k}}}_{Radar,Fd}$ is determined as

$$\tilde{\vec{\mathbf{k}}}_{Radar,Fd} = \cos\tilde{\theta}_{optical}\vec{\mathbf{k}}_{optical,v} + \sin\tilde{\theta}_{optical}\vec{\mathbf{k}}_{optical,u} \tag{16}$$

$$\min_{\alpha,\beta,L} \left(\vec{\mathbf{k}}_{Radar,R} \cdot \vec{\mathbf{l}} - \hat{r}\right)^2 + \left(\vec{\mathbf{k}}_{Optical,U} \cdot \vec{\mathbf{l}} - \hat{u}\right)^2 + \left(\vec{\mathbf{k}}_{\text{Optical},V} \cdot \vec{\mathbf{l}} - \hat{v}\right)^2 \tag{9}$$

$$\begin{aligned} \frac{\vec{\mathbf{k}}_{Radar,Fd} \cdot \vec{\mathbf{l}}_{optical,1}}{\vec{\mathbf{k}}_{Radar,Fd} \cdot \vec{\mathbf{l}}_{optical,2}} &= \frac{(\cos\theta_{optical}\vec{\mathbf{k}}_{optical,v} + \sin\theta_{optical}\vec{\mathbf{k}}_{optical,u}) \cdot (v_1\vec{\mathbf{k}}_{optical,v} + u_1\vec{\mathbf{k}}_{optical,u})}{(\cos\theta_{optical}\vec{\mathbf{k}}_{optical,v} + \sin\theta_{optical}\vec{\mathbf{k}}_{optical,u}) \cdot (v_2\vec{\mathbf{k}}_{optical,v} + u_2\vec{\mathbf{k}}_{optical,u})} \\ &= \frac{\cos\theta_{optical}v_1 + \sin\theta_{optical}u_1}{\cos\theta_{optical}v_2 + \sin\theta_{optical}u_2} \end{aligned} \tag{14}$$

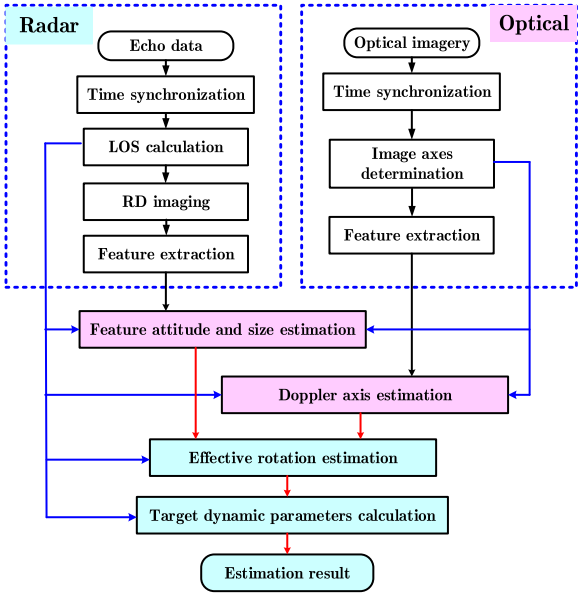

Fig. 4. The flowchart of the proposed algorithm.

After that, the estimated Doppler vector is substituted to Eq. (12) to estimate the equivalent rotation speed of LOS in the current CPI.

$$\begin{cases} \omega_{eff}\tilde{\vec{\mathbf{k}}}_{Radar,Fd}\cdot\tilde{\vec{\mathbf{l}}}_1=\hat{d}_1 \\ \omega_{eff}\tilde{\vec{\mathbf{k}}}_{Radar,Fd}\cdot\tilde{\vec{\mathbf{l}}}_2=\hat{d}_2 \end{cases} \tag{17}$$

It is converted to the following optimization.

$$\min_{\omega_{eff}}\left(\omega_{eff}\tilde{\vec{\mathbf{k}}}_{Radar,Fd}\cdot\tilde{\vec{\mathbf{l}}}_1-\hat{d}_1\right)^2+\left(\omega_{eff}\tilde{\vec{\mathbf{k}}}_{Radar,Fd}\cdot\tilde{\vec{\mathbf{l}}}_2-\hat{d}_2\right)^2 \tag{18}$$

At last, the rotation of the target is determined with the optimal parameters $\tilde{\vec{\mathbf{k}}}_{Radar,Fd}$ and $\tilde{\omega}_{eff}$.

$$\tilde{\vec{\mathbf{w}}}_{eff}=\tilde{\omega}_{eff}\tilde{\vec{\mathbf{k}}}_{Radar,Fd}\times\frac{\vec{\mathbf{w}}_{\mathrm{LOS}}}{\left|\vec{\mathbf{w}}_{\mathrm{LOS}}\right|} \tag{19}$$

$$\vec{\mathbf{w}}_{\mathrm{rot}}=\tilde{\vec{\mathbf{w}}}_{eff}-\vec{\mathbf{w}}_{\mathrm{LOS}}=\tilde{\omega}_{eff}\tilde{\vec{\mathbf{k}}}_{Radar,Fd}-\vec{\mathbf{w}}_{\mathrm{LOS}} \tag{20}$$

where $\times$ is the cross product between two vectors.

III. The Dynamic Estimation Algorithm Based on Synchronized Optical-and-Radar Images

The dynamic estimation of spin satellites is comprised of four components: image preprocessing, feature extraction, target attitude estimation, and spin parameter estimation. The flow of the proposed method is depicted in Fig. 4, and the detailed steps are below.

- Step 1: For the joint utilization of radar and optical images, time synchronization is executed according to the tracking data in the observation systems.
- Step 2: In order to retrieve the 3D observation geometry, the radar LOS sequence is calculated; meanwhile the image axes of optical images are also determined.
- Step 3: The projection lengths of typical structural features, which are located in four dimensions (including the range, Doppler, vertical and horizontal axes), are extracted in the synchronized optical-and-radar images.
- Step 4: Combined with radar LOS and optical calibration information, the extracted range, vertical and horizontal lengths are substituted into optimization (9) to estimate the instantaneous attitude vectors and 3D lengths of typical structural features.
- Step 5: Combined with radar LOS and optical calibration information, the extracted Doppler, vertical and horizontal lengths are used to determine the unit vector of Doppler axis according to optimization (15).
- Step 6: With the accommodation of the above estimation result, the extracted Doppler information is substituted into optimization (18) to determine the effective rotation speed.
- Step 7: After considering the radar LOS change caused by target trajectory, the dynamic parameters of target spin motion are obtained according to Eqs. (19)-(20).

The key steps of the proposed approach are discussed in following subsections.

A. Image Preprocessing

The synchronization of the optical-and-radar observation is an essential prerequisite for the target dynamic estimation in this work. It means that the optical imaging moment ought to be exactly at the central moment of the current radar CPI. After that, the optical image resolution and direction vectors of vertical and horizontal axes are obtained during the optical calibration [34]–[36], while the resolutions of radar imagery needs to be calculated by the radar LOS sequence.

In practical applications, the radar LOS sequence (including azimuth and elevation angles) is usually loaded from the radar tracking system, and handed with the atmosphere correction. Then, according to the radar LOS sequence, the radar echo data is divided and RD imaging is performed to generate high-resolution ISAR imagery. Different from other imaging works [37]–[39], this paper preserves the image Doppler information without the azimuth scaling. The reason is that the angular accumulation of relative rotation between target and radar cannot be determined if the target spin motion is unknown. Thus, the resolutions of acquired RD imagery are expressed as

$$\Delta r=c/2f_s \tag{21}$$

$$\Delta f_d=1/\Delta\mathrm{T} \tag{22}$$

where, f_s refers to the radar sampling frequency, ΔT represents the time accumulation of the current image and c denotes the speed of light.

Moreover, during the preprocessing period, LOS changing component $\vec{\mathbf{w}}_{\mathrm{LOS}}$ is also calculated by using the radar LOS sequence according to Eq. (3). It will be applied in the determination of target dynamic parameters in the last step.

B. Feature Extraction

In this work, four-dimensional information of each structural feature is to be extracted from the radar and optical

images: the projected lengths on range and Doppler axes in the radar image, and the projected lengths on vertical and horizontal axes in the optical image. It is an effective approach to applying polygon fitting, morphological processing, and other relevant image processing techniques to achieve automatic feature extraction [40]. For example, a parallelogram structural feature is extracted by Radon transform acquiring the two-dimensional orientation information of the solar wing in Ref. [21]. Different from the optical image, the radar scattering sensitivity to the radar line of sight would lead to amplitude fluctuation and edge discontinuity of the radar image, which is usually referred as the angular glint phenomenon [21]. It is the fact that keeping correct structure extraction among a large number of radar images is not an easy task. As a result, manual assistance is suggested in the radar-and-optical fusion process. Another fact should be emphasized that, veracity of linear feature length extraction degrades the attitude estimation of the target dynamic, which will be investigated in the experimental part.

C. Parameter Estimation Algorithm

Inspired by the behavior of birds, the particle swarm optimization (PSO) algorithm is a stochastic intelligent method to search the optima [31]–[33]. In this work, it is adopted to solve the instantaneous attitude vectors and 3D lengths of typical features, optimization (9), and also for the parameter estimation of optimizations (15) and (18).

Take optimization (9) as an instance. The solution of minimization (9) is defined as the particle position in PSO.

$$X_i = (\alpha, \beta, L)^T \tag{23}$$

For each structural feature, the fitness function of minimization is defined as Eq. (24), shown at the bottom of this page.

During the process of PSO, the particle's position and velocity are updated according to the swarm search and particle search experiences iteratively. The swarm search experience refers to the best position $Gbest$ found by the swarm, and the particle search experience refers to the best position $Pbest$ found by the particle. The updating rules are given as Eqs. (25)-(26), shown at the bottom of this page.

A brief flow of PSO is given as follows.

- Step 1: Set the maximum iteration and minimum move distance. Generate a particle swarm by random sampling of the solution space of the optimization.
- Step 2: Search the $Gbest$ and $Pbest$ with the fitness function in the current swarm.
- Step 3: Update the position and velocity of each particle according to Eqs. (25)-(26).
- Step 4: Update the fitness value of each particle, and find the $Gbest$ and $Pbest$ in the new swarm. Then, calculate the move distances between the current and former $Gbest$ and $Pbest$. If the maximum iterations or minimum move criterion of the best position is satisfied, break up the current iteration and turn to Step 5; otherwise, turn to Step 3.
- Step 5: Output the position of the ideal particle $\tilde{X}$.

D. Target Dynamic Estimation

1) Absolute Attitude Estimation: As mentioned in Section II.B, the observation geometry of the satellite ought to be determined before estimating the target dynamic parameters. Concretely, three axes: the range axis in the radar imaging plane and the vertical and horizontal axes in the optical imaging plane, are recorded during the observation while the Doppler axis is still unknown and directly related to target dynamic parameters. Therefore, it needs at least two different structural features to solve the Doppler axis vector according to optimization (15). In practical applications, the more structural features this optimization adopts, the more precise the estimation result is.

2) Spin Parameter Estimation: With the feature 3D lengths estimated in the former subsection, the Doppler information of these structural features is utilized further to search the solution of ω_{eff} according to optimization (18), which also can be regarded as the azimuth scaling in radar imagery. Once geometrical parameters $\vec{\mathbf{k}}_{Radar,Fd}$ and ω_{eff} are acquired, the effective LOS change is completely determined. By deducting the change contribution of the relative rotation between the radar and the satellite position in orbit, target dynamic parameters, the spin speed and shaft, is calculated according Eqs. (19)-(20).

Besides, an important prerequisite of the proposed approach lies in that, at least two structural features are necessary for the successful dynamic estimation using the instantaneous optical-and-radar images. As the crux of the proposed algorithm, the elimination of the spinning velocity variable ω_{eff} in Eq. (14) relies on the Doppler feature of two independent structures. When there is only one linear feature available,

$$J = \left(\vec{\mathbf{k}}_{Radar,R} \cdot \vec{\mathbf{l}} - \hat{r}\right)^2 + \left(\vec{\mathbf{k}}_{Optical,U} \cdot \vec{\mathbf{l}} - \hat{u}\right)^2 + \left(\vec{\mathbf{k}}_{\mathrm{Optical},V} \cdot \vec{\mathbf{l}} - \hat{v}\right)^2 \tag{24}$$

$$V_i\,(t+1) = a_0 V_i\,(t) + a_1 rand_1\,(pBest - X_i\,(t)) + a_2 rand_2\,(GBest - X_i\,(t)) \tag{25}$$

$$X_i\,(t+1) = X_i\,(t) + V_i\,(t) \tag{26}$$

where $V_i\,(t)$ and $X_i\,(t)$ are the velocity and position of the ith particle in the iteration t; a_1 and a_2 are two learning rate weights that balance contributions of the self-cognitive and social influence, in this work it is set that $a_1 = a_2$; $rand_1$ and $rand_2$ are two random parameters uniformly distributed within [0, 1]; $a_0$is the inertia weight, and a relatively large inertia weight is better for the global search while a small weight is better for the local search.

TABLE I
THE MAIN PARAMETERS OF THE RADAR AND OPTICAL IMAGES

Size of a single image	512×512
Radar image range resolution	0.05 m
Center frequency of transmit signal	10 GHz
Pulse repetition frequency	100 Hz
Optical image resolutions	$0.05m \times 0.05m$

single Doppler feature is not enough to perform the variable elimination, leading to estimation failure. It is would be potentially applicable to accounting multiple radar images from different radar observation angles in dealing with this case, which will be investigated in the future work.

IV. EXPERIMENT ANALYSIS

In this paper, the feasibility and superiority of the proposed algorithm will be assessed by three parts simulations. First of all, using TG-I as the example, instantaneous dynamic parameters of the spin satellite is estimated by the proposed algorithm. And the structural characteristics of other three satellites are also investigated to confirm the applicability of the proposed algorithm for most satellites. In the second part, the proposed algorithm is performed in different feature extraction and time synchronization conditions, and a long-term image sequence is investigated to estimate target sequential motion. At the last part, the proposed algorithm is compared with existing methods on the estimation performance and observation requirement.

Simulation Methods: Due to the limitation of the real-measured ISAR and optical images of satellites for public use, the proposed algorithm is investigated with simulation imagery. The observation station is set at Beijing (39.9 N, 116.4 E, 88 m), and the satellite two-line orbital element (TLE) parameters are based on a set of public data, according to which the target orbit altitude was around 400 km in 2016. Optical imagery simulation adopts the ray-tracing algorithm [41], [42], while the simulation of the radar imagery is realized by the fast physical optics (FPO) algorithm [43], [44]. The main parameters of the optical and radar images are given in Table I. The signal-to-noise ratio (SNR) of each ISAR image is set to be 10 dB.

A. The Instantaneous Dynamic Estimation of TG-I

To exemplify the proposed algorithm, TG-I is adopted as the observation target in this subsection. The 3D model of TG-I is presented in Fig. 5. The synchronized optical-and-radar images at a particular moment are shown in Fig. 6. During the imaging period, TG-I spacecraft is set to spin around a certain shaft at a constant rotation speed. Two typical structural features of the target, the solar wing and spacecraft body, are extracted in this pair of images (marked green and red, respectively). With the LOS and optical calibration information, three-dimensional lengths, which are extracted on range, vertical and horizontal axes, are applied to estimate the absolute attitude vectors and lengths of these features according to optimization (9).

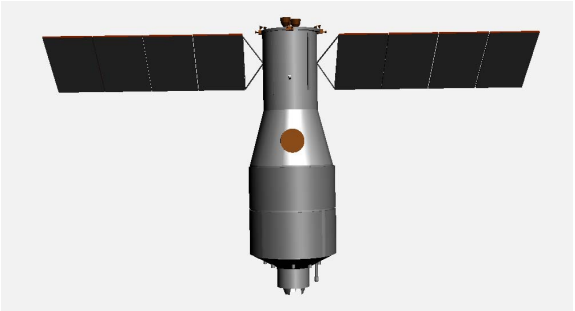

Fig. 5. The 3D model of TG-I Spacecraft.

The estimation results are listed in Table II. As it can be seen, the numerical estimation results are close to the true values.

After that, beside the extracted lengths on vertical and horizontal axes of the optical image, Doppler information of these structural features is also substituted into optimization (15) to estimate the unit vector of Doppler axis in the current CPI. According to optimization (18), once the direction of Doppler axis is determined, the effective rotation speed can be estimated as well. At last, the estimated rotation results are used to calculate the dynamic parameters of the target according to Eqs. (19)-(20). The comparison between the estimation results of dynamic parameters and true values is listed in Table II, and a visual estimation result is given in the target Cartesian coordinates, as shown Fig. 7. By the comparisons of estimation and true values in the table, the veracity of the proposed algorithm is confirmed.

The algorithm is also investigated in another CPI to confirm its feasibility in different CPI conditions. The optical-and-radar images are plotted in Fig. 8, and the target instantaneous dynamic parameters in this moment are given in Table. III. The experiment results illustrate the feasibility of the proposed algorithm in the different CPIs. In practical applications, the CPI of ISAR imaging needs to change with the different observation geometry for acquiring the high-resolution and well-focused radar image. The reason is that the image quality impacts the feature extraction precision directly.

Besides, in order to illustrate the applicability of the proposed algorithm in most tasks, other satellites are also investigated in this paper, including the composition of RadarSats, Mars Reconnaissance Orbiter (MRO) and Rosetta. The structural characteristics of these targets are representative in various applications, and their 3DS models can be loaded on the NASA website (https://nasa3d.arc.nasa.gov/models). As shown in Fig. 9, there are always two or three typical features that can be observed in the synchronized optical-and-radar images (all marked green), and expressed with different pointing vectors. Therefore, by adopting the proposed method, the dynamic estimation of most satellites is available in practical tasks, if there are at least two typical structural features can be extracted synchronously.

B. Performance Investigation

1) Error Analysis: In this work, the extraction precision of typical structural features is the major factor affecting

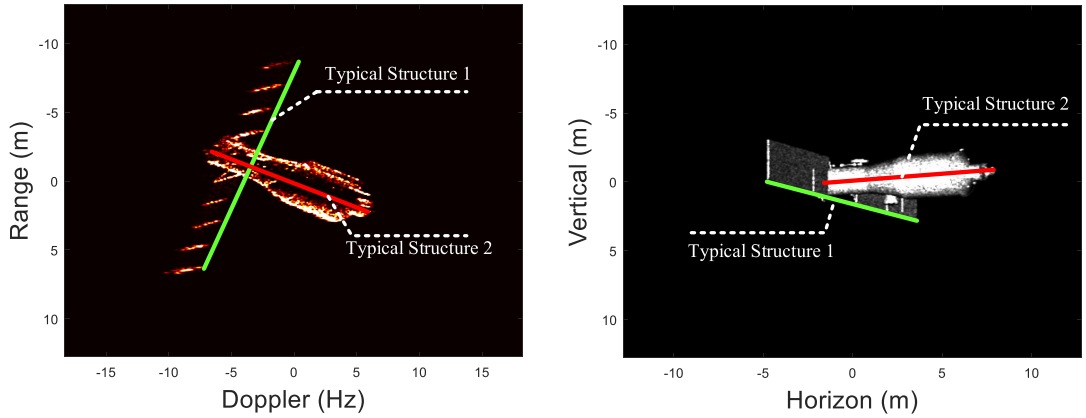

Fig. 6. The synchronized optical-and-radar images of TG-I at a particular moment. (left: The ISAR image; right: The optical image).

TABLE II
THE STATE ESTIMATION RESULTS OF TYPICAL STRUCTURAL FEATURES IN A CERTAIN CPI

Parameter	Estimation value	True value	Error
The attitude vector of structural typical feature 1	(0.2875,-0.1707,0.9425)	(0.2962,-0.1710,0.9397)	0.5255 degrees
The length of typical structural feature 1	16.1271 m	16.0000 m	0.1271 m
The attitude vector of typical structural feature 2	(0.4961,0.8682,0.0083)	(0.5000,0.8660,0)	0.5388 degrees
The length of typical structural feature 2	10.3029 m	10.4000 m	0.0971 m
Fd axis vector	(0.7475,0.4910,-0.4475)	(0.7236,0.5228,-0.4505)	2.2860 degrees
Effective rotation speed	0.0226rad/s	0.0218rad/s	0.0008 rad/s
Target spin shaft vector	(0.9439,-0.1452,-0.2967)	(0.9451,-0.1094, -0.3078)	2.1512 degrees
Target spin speed	0.0146rad/s	0.0141rad/s	0.0005 rad/s

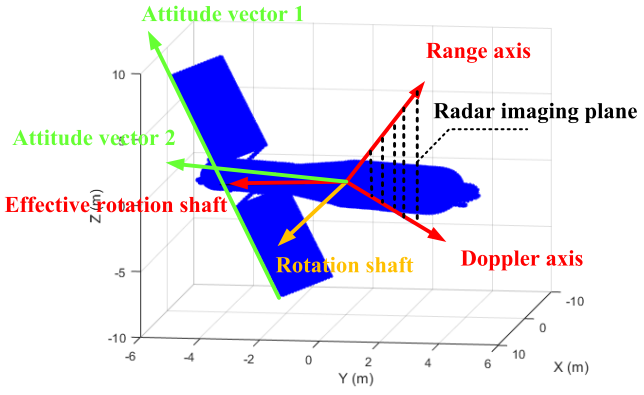

Fig. 7. The visual estimation results in the target Cartesian coordinates.

the performance of the target dynamic estimation. In order to investigate the sensitivity of the proposed algorithm against extraction bias error, dynamic estimation experiment is repeated in different extraction error conditions for these two structural features. In each case, the target is projected with three different poses in optical-and-radar images. Reflecting the estimation error in three steps, the length estimation of typical structural feature 1, Doppler axis and target spinning speed are chosen from attitude estimation results, and averaged to evaluate the performance of the proposed algorithm. From the error curves in Fig. 9, the robustness of the proposed algorithm is confirmed. Even when the extraction error reaches 5 pixels, the estimation precision levels out at an acceptable level (0.15 m, 3 degrees, 0.0004 rad/s).

As mentioned in Section.III A, the synchronization of optical and radar images is an essential prerequisite for the target dynamic estimation in this work. The synchronization of optical and radar observation relies on the GPS time transfer system in ground-based radar and optical sensors. And its effect on the final estimation should be considered under the practical spin speed of LEO satellite. Normally, the time record precision of GPS time transfer system arrives at 10^{-3} seconds [45]. And from the practical works published by the FGAN Lab and International Laser Ranging Service [1], [46], the spin period of spin satellite nears to 160 seconds. Assume there are 10^{-2}-second delays, the changes of target attitude are small in the image, as shown in Fig. 11.

From left to right, the time delays of optical images in Fig. 11 are 0 second, 0.01 second and 0.05 second, respectively. As shown in the figure, the target attitudes are closed among these three frames, and the difference of feature extraction is below 2 pixels in the image. With these images, the dynamic estimation results are given and compared in Table IV. As we can see, the estimation results in these three cases have the similar precision. That is to say that when the tracking data of radar and optical sensors is available, the effect

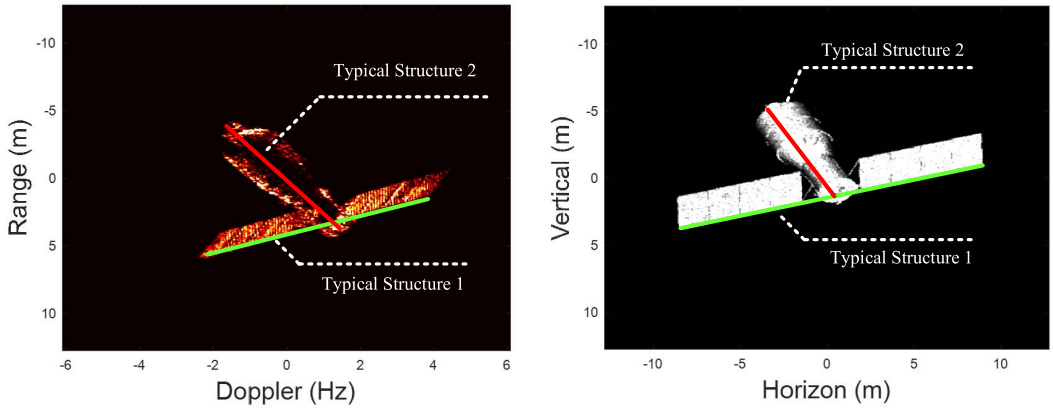

Fig. 8. The synchronized optical-and-radar images. (Left: The ISAR image; right: The optical image).

TABLE III
THE STATE ESTIMATION RESULTS OF TYPICAL STRUCTURAL FEATURES IN ANOTHER CPI

Parameter	Estimation value	True value	Error
The attitude vector of structural typical feature 1	0.4330,-0.7313,0.5271	(0.4240,-0.7344,0.5299)	0.5669 degrees
The length of typical structural feature 1	15.8991 m	16.0000 m	0.1009 m
The attitude vector of typical structural feature 2	(0.8603,0.5097,0.0040)	(0.8660,0.5000,0)	0.6839 degrees
The length of typical structural feature 2	10.3969 m	10.4000 m	0.0031 m
Fd axis vector	(0.1288,0.9916,-0.0089)	(0.1335,0.9908,-0.0213)	0.7628 degrees
Effective rotation speed	0.0074 rad/s	0.0072rad/s	0.0002 rad/s
Target spin shaft vector	(0.4390,0.2715,0.8565)	(0.4203,0.2814,0.8626)	1.2667 degrees
Target spin speed	0.0067 rad/s	0.0066rad/s	0.0001 rad/s

of the time synchronization is limited compared with that of the feature extraction error.

2) The Dynamic Estimation of TG-I in a Long-Term Image Sequence: Drawing on the experience of observations in Refs. [1], [10]–[12], high-resolution and stationary ISAR imaging for spin satellites is attainable in most practical cases, meaning that the premise for the radar imaging model, the imaging plane needs to be approximated to a plane, is plausible. Under this conclusion, the sequential motion is described as the target is spinning around a definite rotation shaft at a constant speed during each imaging CPI, while the rotation shaft and speed are not fixed over long-term observation. In this experiment, instantaneous target dynamic parameters are estimated independently in 10 instances to reflect target continuous motion during a 100-second observation. The feature extraction error is set at 3 pixels in each estimation.

The estimation results of typical features and of target dynamic parameters are listed in Tables V. In general, all attitude estimation errors of typical structural features are controlled within 3 degrees, while the estimated rotation speed is close to the true value at each moment. However, although the attitude errors of typical structural features are at the same degree, the precision of length estimation is different between these two features. The reason is that the true 3D length of typical structural feature 1 (16 m) is much longer than that of typical structural feature 2 (10.4 m). Therefore, under the same condition of feature extraction, the length estimation of typical structural feature 1 is more accurate. From the estimation results in Table V, another experiential conclusion is drawn that the rotation of target spin shaft affects the dynamic estimation. Theoretically, the proposed algorithm is performed independently at each moment without knowledge of the target spin pattern. As a result, it ought to be estimated with similar precision when the algorithm is implemented with different spin patterns. However, compared with the results in Experiment B. 1), the error of target spinning speed increases at a 0.001rad/s level with the change of target spin parameters. This can be accounted for by recognizing that besides the target attitude, the performance of the proposed algorithm is influenced by the relationship between the target spin motion and the radar imaging plane.

C. Comparison Experiment

In order to demonstrate the superiority of the proposed algorithm, the attitude estimation performances of the proposed method and the image sequence interpretation method in Ref. [21] are compared. In the following experiments, the observation geometry of sensors and the on-orbit satellite is set identically. As shown in Fig. 12, five CPIs are chosen in the LOS parameter sequence. The same five ISAR images are generated according to the observation geometry, while optical images are also simulated simultaneously. Extracted by the same image processing, the structure features are used

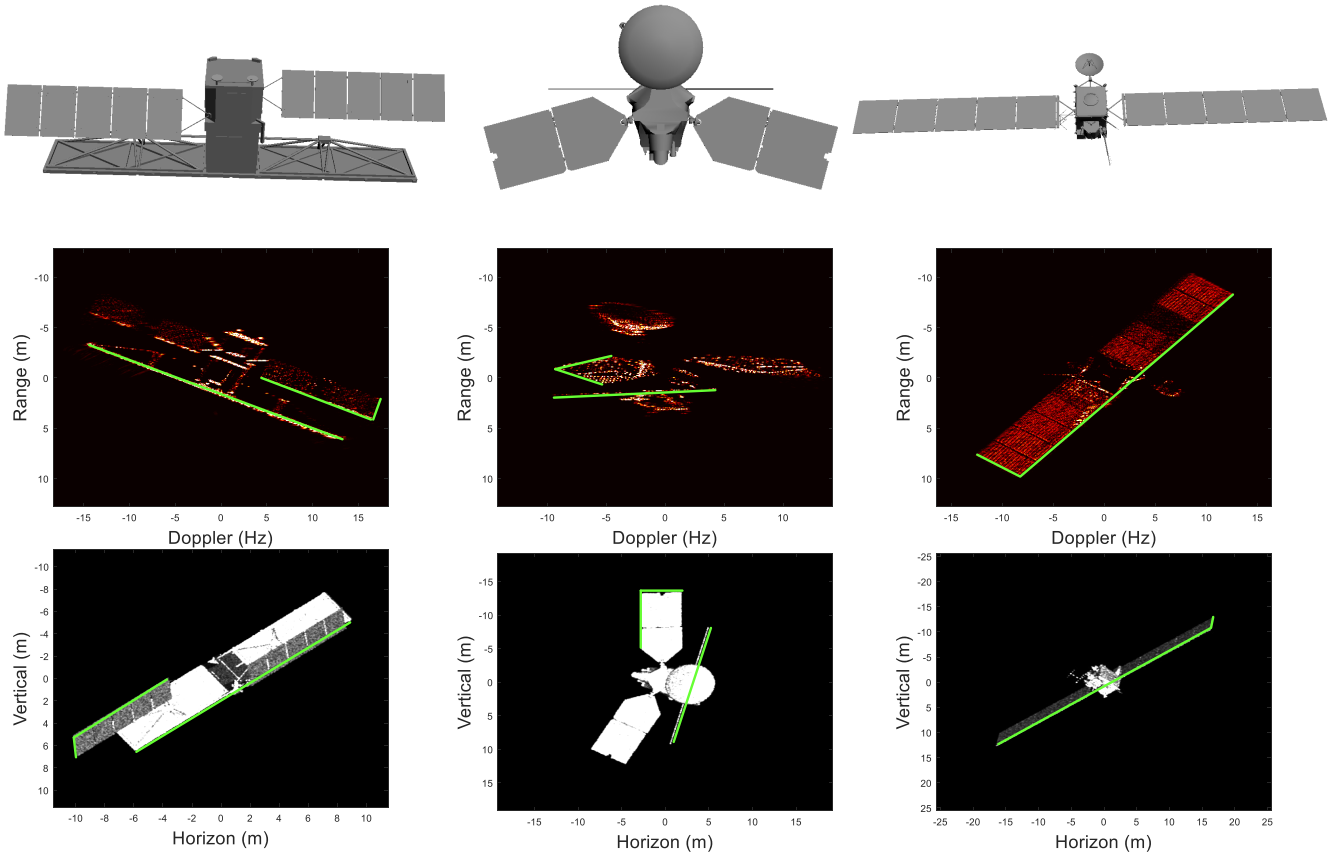

Fig. 9. The synchronized optical-and-radar images of different satellites (First row (from left to right): 3D models of the RadarSat composition, MRO and Rosetta; Second row: ISAR images; Third row: optical images).

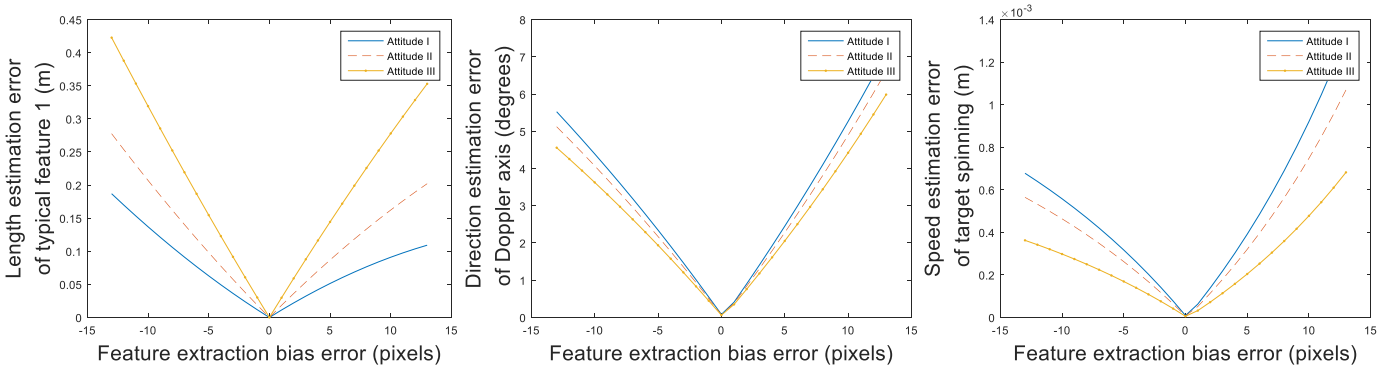

Fig. 10. The curves of estimation error change in different conditions of feature extraction.

to achieve the attitude estimation of the target by the two algorithms, respectively. And their results are compared in a quantitative way.

In the first experiment, the satellite is assumed in a stable state, such as three-axis stability on orbit. Both the two algorithms draw the accurate result of its attitude and the lengths of the structures for the attitude stable target, as shown in Table. VI. The difference lies in their observation time for the successful attitude estimation. Implemented by a geometry back-projection optimization with a sequence of ISAR image, the image sequence interpretation algorithm in [21], [22] requires an observation period of more than 100 seconds to assure a correct attitude. With the help of simultaneous optical information, the observation time is cut down to only several seconds, which is a necessary CPI of a single high-resolution ISAR image. It is revealed that, the orthogonality between the radar and optical image planes provides enough information to determine the target attitude instantaneously. Therefore, the time efficiency superiority of the proposed algorithm is demonstrated by comparing with only radar-based algorithm.

In the second comparison experiment, the target attitude is assumed in spinning around a fixed axis at 0.015 rad/s during the observation. The proposed algorithm is performed to

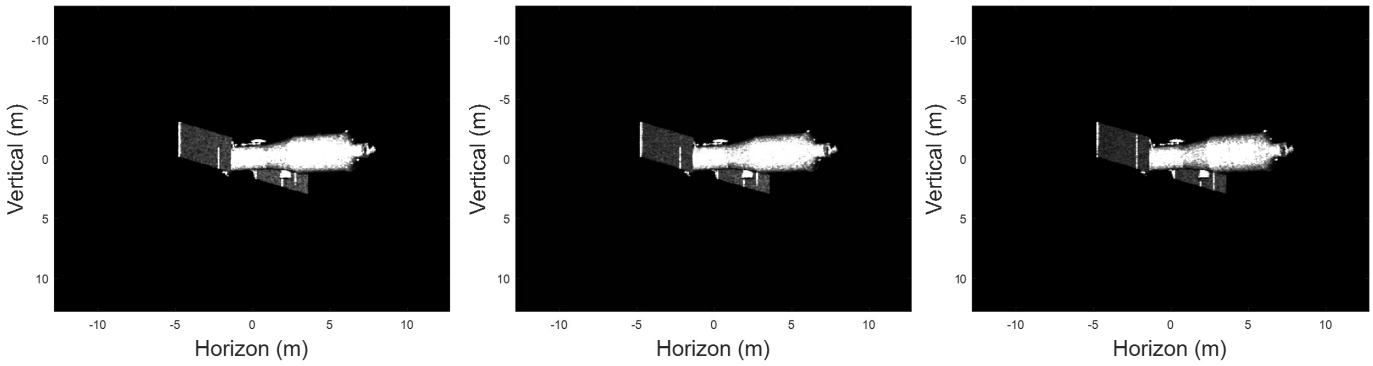

Fig. 11. The optical image in different time delay conditions.

TABLE IV
THE DYNAMIC ESTIMATION RESULTS IN DIFFERENT SYNCHRONIZATION CONDITIONS

Parameter	Estimation value	True value	Error
No Delay			
The attitude vector of structural typical feature 1	(0.2875,-0.1707,0.9425)	(0.2962,-0.1710,0.9397)	0.5255 degrees
The length of typical structural feature 1	16.1271 m	16.0000 m	0.1271 m
The attitude vector of typical structural feature 2	(0.4961,0.8682,0.0083)	(0.5000,0.8660,0)	0.5388 degrees
The length of typical structural feature 2	10.3029 m	10.4000 m	0.0971 m
Fd axis vector	(0.7475,0.4910,-0.4475)	(0.7236,0.5228,-0.4505)	2.2860 degrees
Effective rotation speed	0.0226rad/s	0.0218rad/s	0.0008 rad/s
Target spin shaft vector	(0.9439,-0.1452,-0.2967)	(0.9451,-0.1094, -0.3078)	2.1512 degrees
Target spin speed	0.0146rad/s	0.0141rad/s	0.0005 rad/s
0.01-second Delay			
The attitude vector of structural typical feature 1	(0.2987,-0.1775,0.9377)	(0.2962,-0.1710,0.9397)	0.4110 degrees
The length of typical structural feature 1	16.1713 m	16.0000 m	0.1713 m
The attitude vector of typical structural feature 2	(0.4943,0.8693,-0.0026)	(0.5000,0.8660,0)	0.4051 degrees
The length of typical structural feature 2	10.3390 m	10.4000 m	0.0610 m m
Fd axis vector	(0.7042,0.5480,-0.4515)	(0.7236,0.5228,-0.4505)	1.8229 degrees
Effective rotation speed	0.0212rad/s	0.0218rad/s	0.0006 rad/s
Target spin shaft vector	(0.9440,-0.0744, -0.3216)	(0.9451,-0.1094, -0.3078)	2.1562 degrees
Target spin speed	0.0137rad/s	0.0141rad/s	0.0004 rad/s
0.05-second Delay			
The attitude vector of structural typical feature 1	(0.2943,-0.1690,0.9407)	(0.2962,-0.1710,0.9397)	0.1669 degrees
The length of typical structural feature 1	15.8772 m	16.0000 m	0.1228 m
The attitude vector of typical structural feature 2	(0.4893,0.8721,0.0059)	(0.5000,0.8660,0)	0.7793 degrees
The length of typical structural feature 2	10.3737 m	10.4000 m	0.0263 m
Fd axis vector	(0.7359,0.5073,-0.4484)	(0.7236,0.5228,-0.4505)	1.1433 degrees
Effective rotation speed	0.0223rad/s	0.0218rad/s	0.0005 rad/s
Target spin shaft vector	(0.9443,-0.1304,-0.3021)	(0.9451,-0.1094, -0.3078)	1.2501 degrees
Target spin speed	0.0144rad/s	0.0141rad/s	0.0003 rad/s

extract the dynamic parameters with optical-and-radar images while the existing method [21] only uses the radar images. From the estimation results in Table VII, the ISAR image sequence interpretation algorithm in [21] fails to obtain a correct parameter because of the ISAR image projection change dependent on the spinning motion of the target. However, as shown in Table VII, the proposed algorithm works well since it precisely determines the ISAR projection with the information assistance from the known optical image plane. As a result, the optical-and-radar fusion algorithm is capable of attitude dynamic estimation for spinning targets with only almost instantaneous observation period. In other

TABLE V
THE DYNAMIC ESTIMATION RESULTS

Observation time	CPI 1	CPI 2	CPI 3	CPI 4	CPI 5	CPI 6	CPI 7	CPI 8	CPI 9	CPI 10
Attitude estimation error of typical structural feature 1 (degrees)	0.92	0.92	0.92	0.92	0.92	0.92	0.92	0.92	0.92	0.92
Length estimation error of typical structural feature 1 (m)	0.041	0.038	0.036	0.035	0.034	0.034	0.034	0.035	0.036	0.039
Attitude estimation error of typical structural feature 2 (degrees)	0.94	0.84	0.75	0.75	0.63	0.56	0.48	0.42	0.35	0.28
Length estimation error of typical structural feature 2 (m)	0.195	0.209	0.221	0.221	0.233	0.239	0.244	0.249	0.252	0.255
Pointing estimation error of Doppler axis (degrees)	177.84	178.08	178.36	178.32	178.68	178.84	0.9704	179.25	0.5891	179.58
Estimation error of Effective rotation speed (rad/s)	0.00079	0.00090	0.00094	0.00114	0.00109	0.00116	0.00118	0.00115	0.00122	0.00134
Pointing estimation error of the target spin shaft (degrees)	1.88	2.16	2.30	1.63	1.72	1.50	1.23	0.80	0.47	0.38
Target spin speed (rad/s)	0.0161	0.0149	0.0136	0.0178	0.0149	0.0148	0.0142	0.0145	0.0152	0.0173
Estimated target spin speed (rad/s)	0.0155	0.0142	0.0128	0.0168	0.0139	0.0137	0.0131	0.0134	0.0140	0.0160

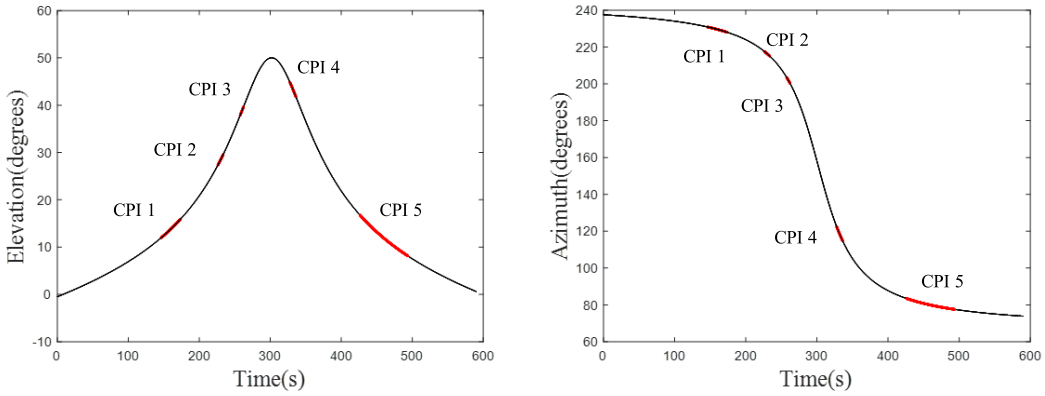

Fig. 12. The LOS parameters of the observation sequence. (Left: the elevation angle sequence; Right:the azimuth angle sequence).

TABLE VI
THE ESTIMATION RESULT COMPARISON FOR STABLE-ATTITUDE TARGETS

Methods	The proposed method					The image sequence interpretation method				
Observation time	CPI 1	CPI 2	CPI 3	CPI 4	CPI 5	CPI 1	CPI 2	CPI 3	CPI 4	CPI 5
Attitude estimation error of typical structural feature 1 (degrees)	0.9192	0.9299	0.9152	0.9051	0.8979	1.3971	1.3971	1.3971	1.3971	1.3971
Length estimation error of typical structural feature 1 (m)	0.0379	0.0500	0.0463	0.0587	0.0658	0.4708	0.4708	0.4708	0.4708	0.4708
Attitude estimation error of typical structural feature 2 (degrees)	0.3016	1.0370	1.1980	1.2211	1.2328	2.7383	2.7383	2.7383	2.7383	2.7383
Length estimation error of typical structural feature 2 (m)	0.2538	0.1773	0.1391	0.1317	0.1275	0.4053	0.4053	0.4053	0.4053	0.4053

words, the proposed optical-and-radar fusion algorithm breaks through the limitations of target stability state assumption. And the assumption is the basis of some existing algorithms in current references, such as [15], [16], [20]–[22]. Therefore, the superiority of the proposed algorithm in dynamic estimation of spinning satellite is confirmed by this experiment.

TABLE VII
THE ESTIMATION RESULT COMPARISON FOR SPIN TARGETS

Method	The proposed method					The image sequence interpretation method				
Observation time	CPI 1	CPI 2	CPI 3	CPI 4	CPI 5	CPI 1	CPI 2	CPI 3	CPI 4	CPI 5
Attitude estimation error of typical structural feature 1 (degrees)	0.8166	0.9033	0.9152	0.9088	0.9026	21.4584	73.6813	76.1643	50.0142	21.4584
Length estimation error of typical structural feature 1 (m)	0.1231	0.0669	0.0112	0.0632	0.0705	9.4278	9.4278	9.4278	9.4278	9.4278
Attitude estimation error of typical structural feature 2 (degrees)	0.7045	0.7845	0.9569	1.2019	1.4322	29.9962	40.1479	52.9452	18.4244	31.5028
Length estimation error of typical structural feature 2 (m)	0.2271	0.2191	0.1972	0.1475	0.0381	8.6523	8.6523	8.6523	8.6523	8.6523

D. Discussion

Overall, the feasibility of algorithm is illustrated in previous experiments, and the influence of two factors (feature extraction accuracy and the geometrical relationship between target dynamic and radar imaging plane) is investigated. Inferred from the measured imagery published by the FGAN Lab [46], a basic premise of the proposed algorithm, the well radar imaging performance of spinning satellites, is satisfied in practical applications. Therefore, we believe the proposed algorithm is suitable for most practical tasks when the quality of optical images is guaranteed.

Additionally, from an information acquisition perspective, the optical-and-radar joint observation itself is superior to the single-sensor model. Compared with the distributed radar network, only one radar and one optical telescope is needed to estimate the dynamic parameters of spin satellites while it needs at least three radars located in different stations to estimate the absolute attitude of the target. The reason is that only the range axis is determined exactly in the single radar observation due to target spin motion. As for two optical telescopes located in different stations, there is no doubt that three-dimensional information of the target can be extracted to estimate its attitude, whereas target dynamic parameters cannot be related to the optical imagery. By contrast, dynamic parameters are estimated from the Doppler information in radar imagery in the optical-and-radar joint observation system. Therefore, we believe the multi-sensor observation frame is more suitable for space monitoring tasks in practice, especially those cases where the observation angle scope is limited. Besides, it also has an extension ability for distributed observation applications, which needs to be further investigated in our future work.

V. CONCLUSION

In this paper, an approach was proposed to estimate the dynamic parameters of spin satellites by interpreting synchronized optical-and-radar images. Based on deduced imaging projection geometry of the optical-and-radar observation, an explicit expression was derived to relate the target dynamic parameters to the observation images. With the accommodation of PSO algorithm, target dynamic parameters were determined in a two-stage optimization. The experiments demonstrated the feasibility of the proposed algorithm. Compared with existing methods, the proposed method overcomes the observation scope limitation and is suitable for most on-orbit satellites without long-term historical data. Additionally, this work also illustrates the superiority of the joint optical-and-radar observation mode in some image interpretation applications.

ACKNOWLEDGMENT

The authors thank the anonymous reviewers for their valuable comments to improve the paper quality.

REFERENCES

[1] D. Kucharski *et al.*, "Attitude and spin period of space debris envisat measured by satellite laser ranging," *IEEE Trans. Geosci. Remote Sens.*, vol. 52, no. 12, pp. 7651–7657, Dec. 2014.
[2] J.-N. Pittet, J. Šilha, and T. Schildknecht, "Spin motion determination of the Envisat satellite through laser ranging measurements from a single pass measured by a single station," *Adv. Space Res.*, vol. 61, no. 4, pp. 1121–1131, 2018.
[3] N. Koshkin, E. Korobeynikova, L. Shakun, S. Strakhova, and Z. H. Tang, "Remote sensing of the EnviSat and Cbers-2B satellites rotation around the centre of mass by photometry," *Adv. Space Res.*, vol. 58, no. 3, pp. 358–371, 2016.
[4] T. Kouyama *et al.*, "Satellite attitude determination and map projection based on robust image matching," *Remote Sens.*, vol. 9, no. 1, p. 90, 2017, doi: 10.3390/rs9010090.
[5] G. Kirchner, W. Hausleitner, and E. Cristea, "Ajisai spin parameter determination using Graz kilohertz satellite laser ranging data," *IEEE Trans. Geosci. Remote Sens.*, vol. 45, no. 1, pp. 201–205, Jan. 2007.
[6] V. Pesce, M. F. Haydar, M. Lavagna, and M. Lovera, "Comparison of filtering techniques for relative attitude estimation of uncooperative space objects," *Aerosp. Sci. Technol.*, vol. 84, pp. 318–328, Jan. 2019, doi: 10.1016/j.ast.2018.10.031.
[7] F. L. Markley, J. Crassidis, and Y. Cheng, "Nonlinear attitude filtering methods," in *Proc. AIAA Guid., Navigat., Control Conf.*, 2005, pp. 15–18.
[8] G. Kirchner, D. Kucharski, and E. Cristea, "Gravity probe-B: New methods to determine spin parameters from kHz SLR data," *IEEE Trans. Geosci. Remote Sens.*, vol. 47, no. 1, pp. 370–375, Jan. 2009.
[9] S. D'Amico, M. Benn, and J. L. Jorgensen, "Pose estimation of an uncooperative spacecraft from actual space imagery," *Int. J. Space Sci. Eng.*, vol. 2, no. 2, pp. 171–189, 2014.
[10] N. O. Gómez and S. J. I. Walker, "Earth's gravity gradient and eddy currents effects on the rotational dynamics of space debris objects: Envisat case study," *Adv. Space Res.*, vol. 56, no. 3, pp. 494–508, 2015.
[11] H.-Y. Lin and C.-Y. Zhao, "An estimation of Envisat's rotational state accounting for the precession of its rotational axis caused by gravity-gradient torque," *Adv. Space Res.*, vol. 61, no. 1, pp. 182–188, 2018.
[12] R. Perrier, E. Arnaud, P. Sturm, and M. Ortner, "Estimation of an observation Satellite's attitude using multimodal pushbroom cameras," *IEEE Trans. Pattern Anal. Mach. Intell.*, vol. 37, no. 5, pp. 987–1000, May 2015.

[13] A. Adnane, Z. A. Foitih, M. A. Si Mohammed, and A. Bellar, "Real-time sensor fault detection and isolation for LEO satellite attitude estimation through magnetometer data," *Adv. Space Res.*, vol. 61, no. 4, pp. 1143–1157, 2018.
[14] J. Rosebrock, "Absolute attitude from monostatic radar measurements of rotating objects," *IEEE Trans. Geosci. Remote Sens.*, vol. 49, no. 10, pp. 3737–3744, Oct. 2011.
[15] M. Avilés, G. Margarit, M. Canetri, and S. Lemmens, "Automated attitude estimation from ISAR images," in *Proc. 7th Eur. Conf. Space Debris*, Darmstadt, Germany, Apr. 2017, pp. 1–13.
[16] S. Sommer *et al.*, "Temporal analysis of ENVISAT's rotational motion," *J. Br. Interplanet. Soc.*, vol. 70, pp. 45–51, Apr. 2017.
[17] L. Carozza and A. Bevilacqua, "Error analysis of satellite attitude determination using a vision-based approach," *ISPRS J. Photogram. Remote Sens.*, vol. 83, pp. 19–29, Sep. 2013.
[18] M. Wang, Y. Zhu, S. Jin, J. Pan, and Q. Zhu, "Correction of ZY-3 image distortion caused by satellite jitter via virtual steady reimaging using attitude data," *ISPRS J. Photogram. Remote Sens.*, vol. 119, pp. 108–123, Sep. 2016.
[19] L. Hong, F. Dai, and H. Liu, "Motion-parameter estimation for precession-with-nutation space targets based on wideband radar measurements," *IEEE Trans. Aerosp. Electron. Syst.*, vol. 52, no. 2, pp. 643–657, Apr. 2016.
[20] K. Suwa, T. Wakayama, and M. Iwamoto, "Three-dimensional target geometry and target motion estimation method using multistatic ISAR movies and its performance," *IEEE Trans. Geosci. Remote Sens.*, vol. 49, no. 6, pp. 2361–2373, Jun. 2011.
[21] Y. Zhou, L. Zhang, Y. Cao, and Z. Wu, "Attitude estimation and geometry reconstruction of satellite targets based on ISAR image sequence interpretation," *IEEE Trans. Aerosp. Electron. Syst.*, vol. 55, no. 4, pp. 1698–1711, Aug. 2019.
[22] Y. Zhou, L. Zhang, and Y. Cao, "Attitude estimation for space targets by exploiting the quadratic phase coefficients of inverse synthetic aperture radar imagery," *IEEE Trans. Geosci. Remote Sens.*, vol. 57, no. 6, pp. 3858–3872, Jun. 2019.
[23] J. T. Mayhan, M. L. Burrows, K. M. Cuomo, and J. E. Piou, "High resolution 3D 'snapshot' ISAR imaging and feature extraction," *IEEE Trans. Aerosp. Electron. Syst.*, vol. 37, no. 2, pp. 630–642, Apr. 2001.
[24] D. Y. Kim and M. Jeon, "Data fusion of radar and image measurements for multi-object tracking via Kalman filtering," *Inf. Sci.*, vol. 278, pp. 641–652, Sep. 2014.
[25] C. Pohl and J. L. Van Genderen, "Review article multisensor image fusion in remote sensing: Concepts, methods and applications," *Int. J. Remote Sens.*, vol. 19, no. 5, pp. 823–854, 1998.
[26] G. Fasano, D. Accardo, A. E. Tirri, A. Moccia, and E. De Lellis, "Radar/electro-optical data fusion for non-cooperative UAS sense and avoid," *Aerosp. Sci. Technol.*, vol. 46, pp. 436–450, Oct./Nov. 2015.
[27] S. Zheng, W. Shi, J. Liu, G. Zhu, and J. Tian, "Multisource image fusion method using support value transform," *IEEE Trans. Image Process.*, vol. 16, no. 7, pp. 1831–1839, Jul. 2007.
[28] F. R. Al-Osaimi, M. Bennamoun, and A. Mian, "Spatially optimized data-level fusion of texture and shape for face recognition," *IEEE Trans. Image Process.*, vol. 21, no. 2, pp. 859–872, Feb. 2012.
[29] B. Waske and S. V. D. Linden, "Classifying multilevel imagery from SAR and optical sensors by decision fusion," *IEEE Trans. Geosci. Remote Sens.*, vol. 46, no. 5, pp. 1457–1466, May 2008.
[30] Y. Byun, J. Choi, and Y. Han, "An area-based image fusion scheme for the integration of SAR and optical satellite imagery," *IEEE J. Sel. Topics Appl. Earth Observ. Remote Sens.*, vol. 6, no. 5, pp. 2212–2220, Oct. 2013.
[31] J. Kennedy and R. Eberhart, "Particle swarm optimization," in *Proc. IEEE Int. Conf. Neural Netw.*, vol. 4, Nov. 1995, pp. 1942–1948.
[32] J. Saeedi and K. Faez, "A new pan-sharpening method using multiobjective particle swarm optimization and the shiftable contourlet transform," *ISPRS J. Photogram. Remote Sens.*, vol. 66, pp. 365–381, May 2011.
[33] X. Jin *et al.*, "Winter wheat yield estimation based on multi-source medium resolution optical and radar imaging data and the AquaCrop model using the particle swarm optimization algorithm," *ISPRS J. Photogram. Remote Sens.*, vol. 126, pp. 24–37, Apr. 2017.
[34] Y. Ma, S. Soatto, S. S. Sastry, and J. Kosecká, *An Invitation to 3-D Vision: From Images to Geometric Models*. Cambridge, MA, USA: Springer, 2012.
[35] T. Rahman and N. Krouglicof, "An efficient camera calibration technique offering robustness and accuracy over a wide range of lens distortion," *IEEE Trans. Image Process.*, vol. 21, no. 2, pp. 626–637, Feb. 2012.
[36] L. O'Gorman and G. Yang, "Orthographic perspective mappings for consistent wide-area motion feature maps from multiple cameras," *IEEE Trans. Image Process.*, vol. 25, no. 6, pp. 2817–2832, Jun. 2016.
[37] Z. Bao, M. Xing, and T. Wang, *Radar Imaging Technology*. Beijing, China: Publishing House of Electronics Industry, 2005, pp. 24–40.
[38] L. Zhang *et al.*, "Resolution enhancement for inversed synthetic aperture radar imaging under low SNR via improved compressive sensing," *IEEE Trans. Geosci. Remote Sens.*, vol. 48, no. 10, pp. 3824–3838, Oct. 2010.
[39] L. Zhang, Z. Qiao, M. Xing, Y. Li, and Z. Bao, "High-resolution ISAR imaging with sparse stepped-frequency waveforms," *IEEE Trans. Geosci. Remote Sens.*, vol. 49, no. 11, pp. 4630–4651, Nov. 2011.
[40] R. C. Gonzalez and R. E. Woods, *Digital Image Processing*. Beijing, China: Publishing House of Electronics Industry, 2007, pp. 432–435.
[41] S. Auer, S. Hinz, and R. Bamler, "Ray-tracing simulation techniques for understanding high-resolution SAR images," *IEEE Trans. Geosci. Remote Sens.*, vol. 48, no. 3, pp. 1445–1456, Mar. 2010.
[42] K. S. Kulpa *et al.*, "An advanced SAR simulator of three-dimensional structures combining geometrical optics and full-wave electromagnetic methods," *IEEE Trans. Geosci. Remote Sens.*, vol. 52, no. 1, pp. 776–784, Jan. 2014.
[43] A. Boag, "A fast physical optics (FPO) algorithm for high frequency scattering," *IEEE Trans. Antennas Propag.*, vol. 52, no. 1, pp. 197–204, Jan. 2004.
[44] A. F. Garcia-Fernandez, O. A. Yeste-Ojeda, and J. Grajal, "Facet model of moving targets for ISAR imaging and radar back-scattering simulation," *IEEE Trans. Aerosp. Electron. Syst.*, vol. 46, no. 3, pp. 1455–1467, Jul. 2010.
[45] W. Lewandowski and C. Thomas, "GPS time transfer," *Proc. IEEE*, vol. 79, no. 7, pp. 991–1000, Jul. 1991.
[46] *Forscher des Fraunhofer FHR Begleiten Wiedereintritt der Chinesischen Raumstation Tiangong-1*, FGAN Lab, Berlin, German, Mar. 2018. [Online]. Available: https://www.fhr.fraunhofer.de/tiangong- bilder

Yejian Zhou was born in Zhejiang, China, in 1993. He received the B.S. degree in electronic engineering from Xidian University, Xian, China, in 2015, where he is currently pursuing the Ph.D. degree in signal processing with the National Laboratory of Radar Signal Processing. He is also a Visiting Ph.D. student with the Department of Urban Planning and Environment, KTH Royal Institute of Technology. His research interests include ISAR imaging and image interpretation.

Lei Zhang was born in Zhejiang, China, in 1984. He received the Ph.D. degree from Xidian University in 2012. He is currently an Associate Professor with the School of Electronics and Communication Engineering, Sun Yat-Sen University. His research interests are radar imaging (SAR/ISAR) and motion compensation.

Yunhe Cao was born in Anhui, China. He received the B.S., M.S., and Ph.D. degrees from Xidian University, Xi'an, China, in 2001, 2004, and 2006, respectively. He is currently a Professor with the National Laboratory of Radar Signal Processing, Xidian University. His research interests include MIMO radar, digital array radar, adaptive signal processing, and target detection.

Yan Huang received the B.S. degree in electrical engineering and the Ph.D. degree in signal and information processing from Xidian University, Xi'an, China, in 2013 and 2018, respectively. He was a Visiting Ph.D. student with the Electrical and Computer Engineering Department, University of Florida, from September 2016 to July 2017, and with the Electrical and Systems Engineering Department, Washington University in St. Louis, from July 2017 to August 2018. He is currently an Assistant Professor with the State Key Laboratory of Millimeter Waves, Southeast University. His research interests include machine learning, synthetic aperture radar, image processing, and remote sensing.